

THIN  $\text{Cr}_2\text{O}_3$  (0001) FILMS AND Co (0001) FILMS FABRICATION FOR SPINTRONICS

Yuan Cao

Thesis Prepared for the Degree of

MASTER OF SCIENCE

UNIVERSITY OF NORTH TEXAS

December 2015

APPROVED:

Jeffery A. Kelber, Major Professor  
Teresa D. Golden, Committee Member  
Francis D'Souza, Committee Member

Cao, Yuan. Thin Cr<sub>2</sub>O<sub>3</sub> (0001) Films and Co (0001) Films Fabrication for Spintronics.

Master of Science (Chemistry-Analytical Chemistry), December 2015, 37 pp., 10 illustrations, references, 41 titles.

The growth of Co (0001) films and Cr<sub>2</sub>O<sub>3</sub> (0001)/Co (0001) has been investigated using surface analysis methods. Such films are of potential importance for a variety of spintronics applications. Co films were directly deposited on commercial Al<sub>2</sub>O<sub>3</sub> (0001) substrates by magnetron sputter deposition or by molecular beam epitaxy (MBE), with thicknesses of ~1000 Å or 30 Å, respectively. Low Energy Electron Diffraction (LEED) shows hexagonal (1x1) pattern for expected epitaxial films grown at 800 K to ensure the hexagonally close-packed structure. X-ray photoemission spectroscopy (XPS) indicates the metallic cobalt binding energy for Co (2p<sub>3/2</sub>) peak, which is at 778.1 eV. Atomic force microscopy (AFM) indicates the root mean square (rms) roughness of Co films has been dramatically reduced from 10 nm to 0.6 nm by optimization of experiment parameters, especially Ar pressure during plasma deposition. Ultrathin Cr<sub>2</sub>O<sub>3</sub> films (10 to 25 Å) have been successfully fabricated on 1000 Å Co (0001) films by MBE. LEED data indicate Cr<sub>2</sub>O<sub>3</sub> has C<sub>6v</sub> symmetry and bifurcated spots from Co to Cr<sub>2</sub>O<sub>3</sub> with Cr<sub>2</sub>O<sub>3</sub> thickness less than 6 Å. XPS indicates the binding energy of Cr 2p(3/2) is at 576.6 eV which is metallic oxide peak. XPS also shows the growth of Cr<sub>2</sub>O<sub>3</sub> on Co (0001) form a thin Cobalt oxide interface, which is stable after exposure to ambient and 1000 K UHV anneal.

Copyright 2015

By

Yuan Cao

## ACKNOWLEDGEMENTS

First, I wish to acknowledge the help provided by my research advisor, Dr. Jeffry A. Kelber, for his guidance and constructive suggestion. I have benefited in many ways from working with him and his research group.

I wish to extend my appreciation to my committee members, Dr. Golden and Dr. D'Souza; I want to give my special thanks to Dr. M. Sky Driver for his selfless sharing knowledge and many stimulating discussions. I also want to extend my thanks for the support of the Chemistry department for supporting our research from many aspects. I am especially grateful to my parents for their love and support all these years.

Appreciation is extended to Elsevier Journal. The sections 3.2 and 3.3 of the chapter 3 are from previous published paper "Ultrathin chromia films grown with preferential texture on metallic, semimetallic and insulating substrates," *Mater. Chem. Phys.*, vol. 149–150, pp. 113–123, 2015." with Elsevier Journal's permission.

## TABLE OF CONTENTS

ACKNOWLEDGEMENTS.....	ii
LIST OF ILLUSTRATIONS.....	vi
CHAPTERS	
1. INTRODUCTION.....	1
1.1 Background and Theory Introduction.....	1
2. EXPERIMENTAL METHODS.....	3
2.1. Equipment Description: The UHV System.....	3
2.2. Characterization Techniques.....	5
2.2.1 X-ray Photoelectron Spectroscopy (XPS) .....	5
2.22 Low Energy Electron Diffraction (LEED) .....	8
2.3 Film Deposition Method .....	10
2.31 Magnetron Sputter Deposition .....	10
2.32 Molecular Beam Epitaxy (MBE) .....	12
2.33 Atomic Force Microscopy (AFM) .....	14
3. THE EXPERIMENT RESULT .....	16

3.1	Magnetron Sputtering Deposition of Cobalt on Al <sub>2</sub> O <sub>3</sub> (0001) Films .....	16
3.11	Co Surface Roughness Improvement .....	17
3.12	XPS and LEED Analysis .....	19
3.2	MBE of Cr <sub>2</sub> O <sub>3</sub> on Co(0001)/Al <sub>2</sub> O <sub>3</sub> Films .....	22
3.3	Chromia growth on Al <sub>2</sub> O <sub>3</sub> (0001) .....	27
4.	SUMMARY and CONCLUSION .....	29
4.1	Summary .....	29
4.2	Future work .....	30
	REFERENCES .....	31

## LIST OF TABLES

	Page
3.1 List of sample RMS with corresponding experiment parameters after Co magnetron sputtering deposited Co (0001) on $\text{Al}_2\text{O}_3$ . RMS is measured by AFM .....	19

## LIST OF ILLUSTRATIONS

	Page
2.1 UHV system 1 .....	3
2.2 UHV system 2 (PVD Chamber) .....	5
2.3 X-ray photoelectron spectroscopy .....	6
2.4 Photoelectrons with kinetic energy KE is produced by ejected core level electron from x-ray with certain energy hv. ....	7
2.5 Low energy electron diffraction .....	9
2.6 One dimensional model of electron diffraction process .....	10
2.7 Mechanism of magnetron sputtering deposition .....	11
2.8 Molecular beam epitaxy deposition .....	13
2.9 The basic principle of AFM image .....	14
3.1 The AFM image acquired after Co PVD deposition on Al <sub>2</sub> O <sub>3</sub> at 800K for 15mins with (a) plasma power at 50w and Ar pressure at 15mtorr and (b) plasma power at 50w and Ar pressure at 7mT.....	17
3.2 The AFM image acquired after Co PVD deposition on Al <sub>2</sub> O <sub>3</sub> at 800K for 15mins with (a) plasma power at 15w and Ar pressure at 3.5mTorr and (b) plasma power at 10w and Ar pressure at 3.5mT.....	18
3.3 The XPS core level spectra for (a) C(1s), (b) O(1s) and (c) Co(2p) acquired after Co cleaning process. ....	21
3.4 LEED patterns for (a)clean Al <sub>2</sub> O <sub>3</sub> and (b) Co overlayers on Al <sub>2</sub> O <sub>3</sub> ; All LEED patterns acquired at 70 eV beam kinetic energy. ....	21
3.5 (a) Auger electron spectroscopy acquired after 1st Cr MBE/oxidation cycle (solid black trace) and after 2nd Cr MBE/oxidation cycle (open circles), (b) the expanded view of the Cr (LMM)/O (KVV) region. (LMM is an L shell core hole, M shell transi..	22



3.6	The LEED image (a) and line scan (b) after the first chromium deposition/oxidation cycle (roughly 9 Å) on Co (0001). Note the evidence of overlayer mismatch in the line scan. This can be compared with the LEED image (c) and line scan (d) after s.....	23
3.7	The various LEED patterns for chromia overlayers on cobalt: (a) thicker (>11 Å) Cr <sub>2</sub> O <sub>3</sub> on Co; (b) the clean Co substrate; All LEED patterns acquired at 90 eV beam kinetic energy. ....	25
3.8	The XPS core level spectra for Cr 2p (a) and O 1s (b) core levels after Cr <sub>2</sub> O <sub>3</sub> deposition on Co(0001) (see text), and for Cr 2p (c) and O 1s (c) core levels after Cr <sub>2</sub> O <sub>3</sub> deposition on Al <sub>2</sub> O <sub>3</sub> .....	26
3.9	XPS Co 2p spectra of a Cr <sub>2</sub> O <sub>3</sub> (0001)/Co (0001) film after sample transfer/UHV anneal (solid trace) and after a second air exposure/UHV annealing cycle (open cycle). The feature corresponding to the presence of cobalt oxide is marked by an arrow. ....	27
3.10	The various LEED patterns for chromia overlayers on sapphire: (a) Cr <sub>2</sub> O <sub>3</sub> on Al <sub>2</sub> O <sub>3</sub> (b) the clean Al <sub>2</sub> O <sub>3</sub> substrate; All LEED patterns acquired at 90 eV beam kinetic energy.....	28

## CHAPTER 1

### INTRODUCTION

#### 1.1 Background

Chromia ( $\text{Cr}_2\text{O}_3$ ) is a special antiferromagnetic material which is magnetoelectric [1], [2] -- in which the boundary layer magnetization can be switched by applying an electric field (applied voltage), which is of significance for the development of low power spintronics [3]. Compared to magnetic field control of the spin polarization, the electric field control only requires very low voltage and no currents, which can significantly reduce the power consumption and heat dissipation [4], [5]. The Néel temperature of  $\text{Cr}_2\text{O}_3$  is at 307 K [6] which provides a possible route to achieve spintronics at room temperature. Below the Néel temperature, the thermal energy is not high enough to break the magnetic ordering, therefore  $\text{Cr}_2\text{O}_3$  keeps antiferromagnetic ordering. If  $\text{Cr}_2\text{O}_3$  is used as a spin pinning layer for spintronics, the magnetic state of  $\text{Cr}_2\text{O}_3$  can be directly controlled at room temperature without a cooling system. This is a critical step to make practical devices. A special ferromagnetic property has been discovered on  $\text{Cr}_2\text{O}_3$  (0001) surface which is long range ordered regardless of the roughness of the surface [7]. Antiferromagnetic films usually show zero magnetization on the surface due to a very rough surface (The multi magnetic domain states formed on film surface compensating each other) [8]. The fabrication of antiferromagnetic films with magnetically uncompensated surface is very difficult to achieve. However, this is a very important property for spin pinning of antiferromagnetic films to others, especially when used for exchange bias. The magnetic state of the  $\text{Cr}_2\text{O}_3$ (0001) surface has been discovered to be long range ordered even with a very rough surface, which is key for exchange bias formation at the interface with

ferromagnetic material [7], [9]. All these properties above are perfect for spintronics to achieve isothermal voltage control of exchange bias. Therefore, for such applications, it is important to develop a good method for  $\text{Cr}_2\text{O}_3$  ultrathin film fabrication on various substrates.

## CHAPTER 2

### EXPERIMENTAL METHODS

#### 2.1. Equipment Description: The UHV System

In this study, all experiments were performed in ultra high vacuum (UHV), using three separate UHV systems to make use of the broad range of surface analytical tools. System 1 is shown in Fig. 2.1. This UHV system is pumping by the ion pump and turbo pump together, which maintains the working pressure at  $1 \times 10^{-10}$  Torr. This system includes two separate chambers connected by a gate valve.

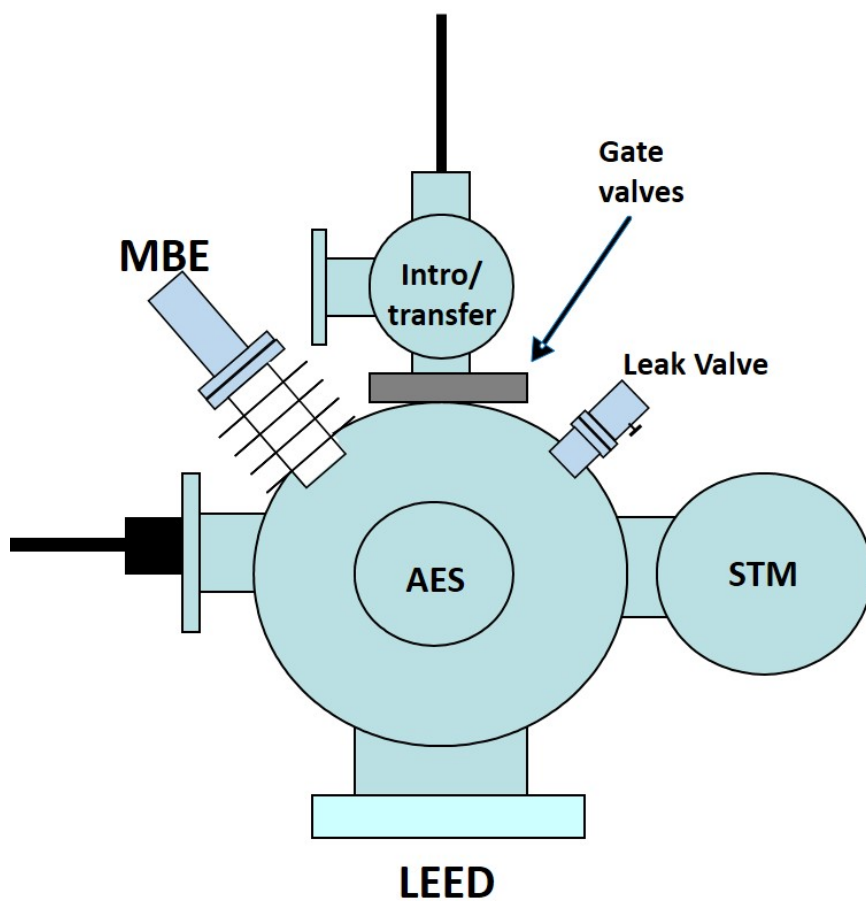


Fig. 2.1 UHV system 1.

The main chamber, which is equipped with analytical tools (Auger electron spectroscopy (AES), low energy electron diffraction (LEED) and scanning tunneling microscope (STM)), is used for sample analysis. Film deposition is performed by an electron-beam (e-beam) evaporator with different sources for molecular beam epitaxy (MBE) deposition in the main chamber. A sample transfer arm equipped in the main chamber with the ability to anneal samples to 1000 K is used to change sample position for different analytical tools and MBE deposition. An intro chamber connected to the main chamber is used for sample loading.

The second system is a magnetron sputtering deposition chamber as shown in Fig. 2.2. This system is pumped by a turbo pump to maintain the working pressure at  $3 \times 10^{-8}$  Torr. A magnetron sputtering gun is used for Physical Vapor Deposition (PVD). Argon and hydrogen gas can be introduced to this system through two leak valves. Ion gauge and Baratron gauge are used for monitoring the system pressure. The butterfly valve is used for isolating or regulating gas flow.

The third chamber is equipped with analytical tools like x-ray photoelectron spectroscopy (XPS) and LEED; it also has abilities for MBE and PVD deposition. The base pressure of this system is maintained at  $1 \times 10^{-10}$  Torr by a turbo pump. This system has the ability to fabricate several in situ stacks of films by both MBE and PVD deposition. The composition and crystal structure of fabricated films can be directly analyzed by XPS and LEED just after deposition.

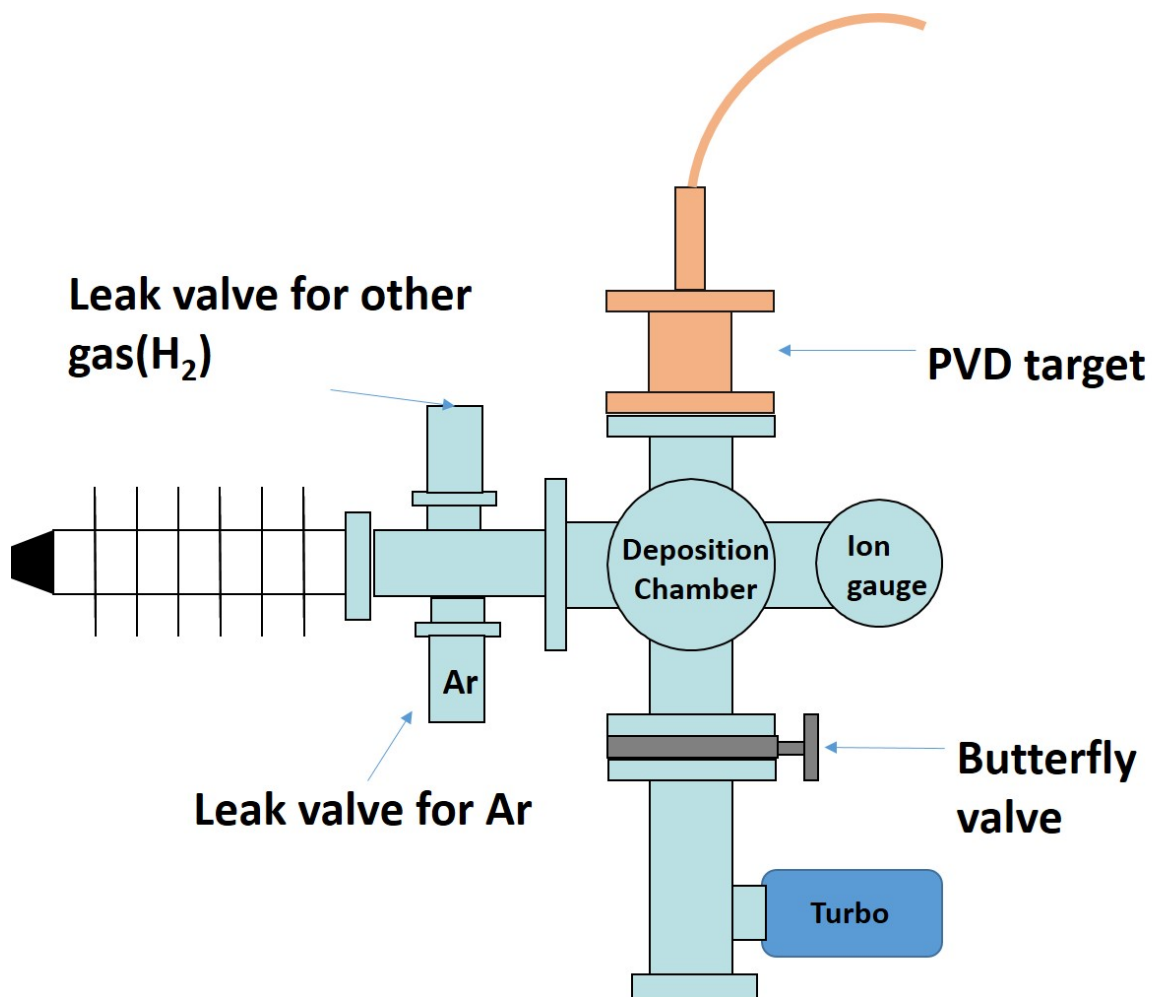


Fig. 2.2 UHV system 2 (PVD Chamber).

## 2.2 Characterization Techniques

### 2.2.1 X-ray Photoelectron Spectroscopy (XPS)

XPS is widely used as an analytical tool for surface study on surface elemental composition and the chemical bonding environments of atoms on an element sensitive bias.

XPS, as shown in Fig. 2.3 has three components.

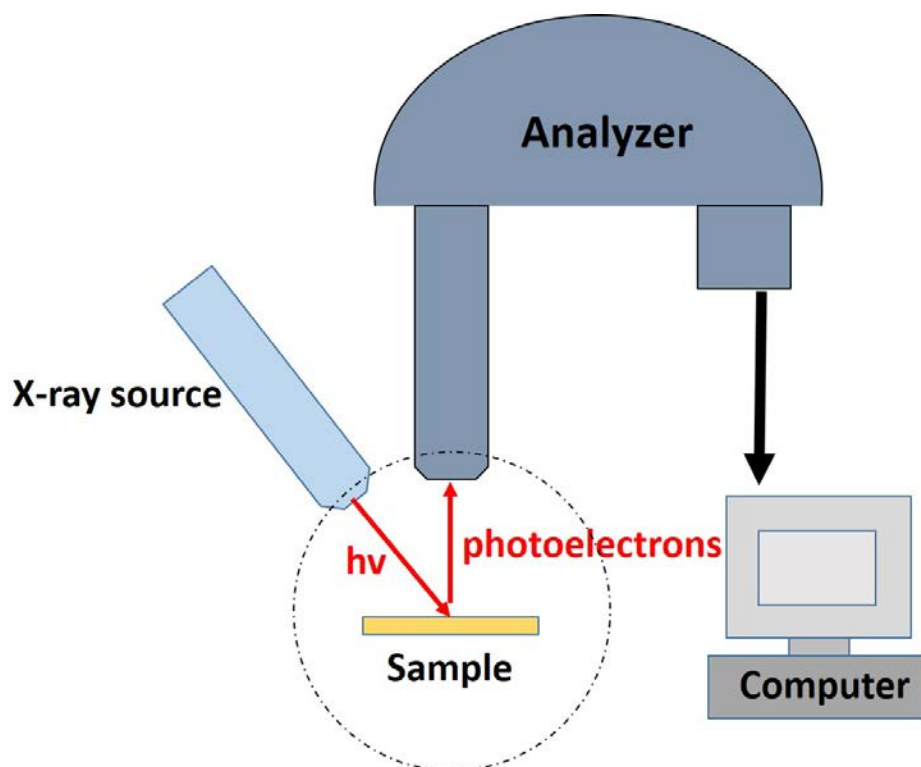


Fig. 2.3 X-ray photoelectron spectroscopy.

A x-ray gun is used as the photon source to produce characteristic x-rays (Mg and Al anodes are usually used to produce x-ray with 1253.6eV and 1486.6eV photon energy) in order to eject core level electrons from the sample surface. A hemispherical analyzer is used to detect the photoelectrons ejected by x-ray from sample surface. After a signal is detected, it is sent to a computer to convert to spectral.

The basic principle of XPS is based on the photoelectric effect (certain materials emit electrons after being exposed to a photon source with high enough photon energy). For XPS, x-rays are used as the photon source to eject core level electrons from the sample. The ejected electrons are called photoelectrons. Once the photoelectrons reach the detector, the analyzer measures the kinetic energy of detected photoelectrons based on energy conservation law. The

binding energy of the electron can be calculated by the equation 2.1

$$BE = h\nu - KE - \Phi \quad [2.1]$$

$\Phi$  is the work function of the analyzer. Because each atom has their characterized binding energy, the elemental content of the sample surface is determined by the binding energy detected from their photoelectrons. The chemical state is determined by the shift binding energy, which is due to the charge transfer and interaction with neighboring atoms.

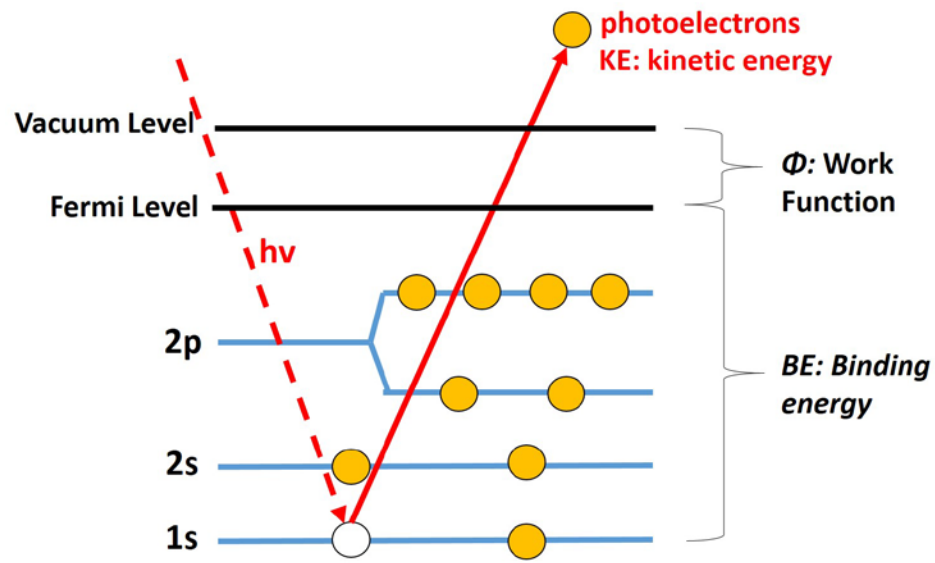


Fig. 2.4 Photoelectrons with kinetic energy KE is produced by ejected core level electron from x-ray with certain energy  $h\nu$ .

XPS can also provide information for the thin film thickness calculation, which is important for quantitative control of thin film in fabrication process; however, it is only an estimation. The thickness calculation is based on the equation 2.2 and 2.3[10].

$$I_B = I_B^\infty e^{-d/\lambda_A(E_B) \cos\theta} \quad [2.2]$$

$$I_A = I_A^\infty [1 - e^{-d/\lambda_A(E_A) \cos\theta}] \quad [2.3]$$



$I_A$  and  $I_B$  are the signal intensities integrated from the corresponding overlayer and substrate peaks;  $I_A^\infty$ ,  $I_B^\infty$  are the atomic sensitivity factors;  $d_A$  is the overlayer thickness; and  $\lambda_A$  is the inelastic mean free path (IMFP) for photoelectrons emitted from substrate through the overlayer. IMFP is calculated from TPP-2M equations [10], [11].  $\Theta$  is the angle between sample surface normal and the detector. With the increase of overlayer thickness, the intensity  $I_B$  increases and  $I_A$  is attenuated by the overlayer. Therefore, the  $d_A$  is determined by the intensity ratio of  $I_B/I_A$  and solved by equation 2.2 and 2.3.

## 2.22 Low Energy Electron Diffraction (LEED)

LEED is a powerful tool for crystal surface structure analysis by acquiring the diffraction pattern of low energy electrons back scattered from the sample surface. It provides two important ways to analyze crystal structure. First is qualitative analysis; the pattern of diffraction spots detected by fluorescent screen provide information of crystal symmetry, domain size, and rotational alignment between the first layer and substrate. Second is quantitative analysis; a  $I/V$  curve which is the plot of the intensity of diffraction spots changes with different beam energy acquired from LEED spectra can provide information of the atomic position.

Fig. 2.5 shows the design of the LEED instrument used in these studies. An electron gun incident perpendicular to sample surface is used to produce well defined low energy electron beams (0 to 200 eV). A fluorescent screen is used to observe diffracted electrons elastic back scattered from crystal as spots. Grids applied with certain potentials are used to screen the secondary electrons inelastic back scattered from the sample.

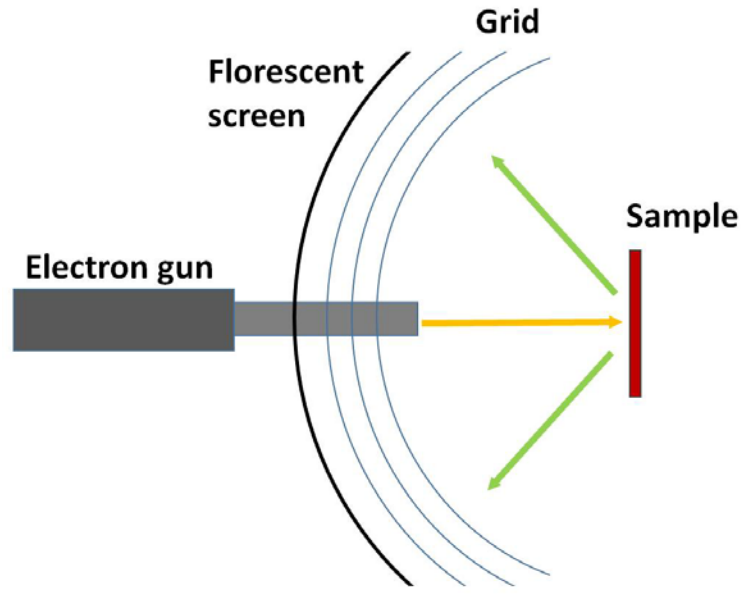


Fig. 2.5 Low energy electron diffraction.

The basic principle of LEED is based on de Broglie relation (Equation 2.4) and Bragg's law (Equation 2.5).

$$\lambda = h/p \quad [2.4]$$

$$d \sin \theta = n\lambda \quad [2.5]$$

For equation 2.4, the electrons from the electron beam can be seen as propagated waves.  $\lambda$  is wavelength,  $h$  is plank constant,  $P$  is the electron momentum.  $P$  can be controlled by changing the acceleration energy of electrons. When the electrons with kinetic energy are in the range from 20eV to 200eV, the wave length of electrons in this range is close to the distance between two adjacent atoms in a crystal which is a necessary condition for the back scattered electron diffraction to happen and are related to the crystal structure.

For Equation 2.5 (Bragg's law),  $n$  is an integral number. When  $d$  is equal to  $n \lambda$ , the electron constructive interference beam will be observed by the detector. This can be

understood by Fig 2.6 which is a one dimensional simple model of electron diffraction process on sample surface. The red arrows point down is an electron beam with certain energy incident perpendicular to the sample surface. The green arrow is elastic backscattered electrons with an angle  $\Theta$  between the sample normal and green arrow. The adjacent atom distance in this crystal is  $a$ . The path difference between two adjacent atoms is  $d$ . In order to let the back scattered electrons have constructive interference with each other and be detected by the fluorescent screen, the path difference  $d$  must be an integral number of electron wavelengths.

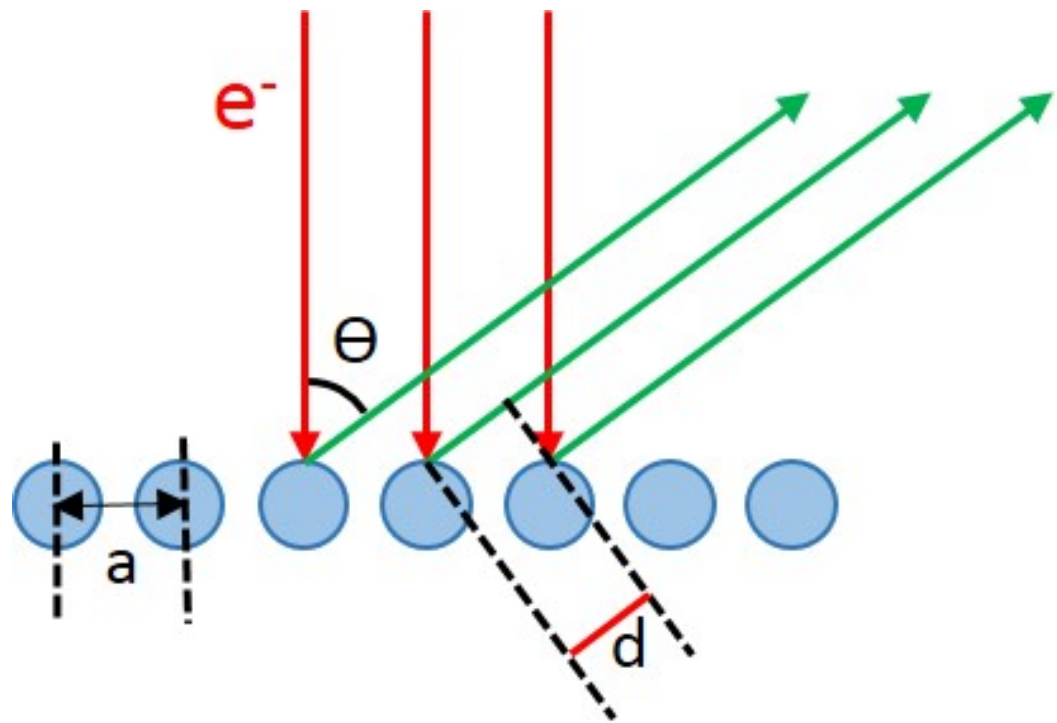


Fig. 2.6 One dimensional model of electron diffraction process.

## 2.3 Film Deposition Method

### 2.31 Magnetron Sputtering Deposition

Magnetron sputter deposition is one of the most common methods of thin film deposition[12]. It is a physical vapor deposition technique. Fig. 2.7 shows the magnetron

sputter deposition process. A target composed with desired material for film deposition is used as a source. Ionized noble gas with high kinetic energy from plasma keeps bombarding the target. After collision with the target, these energetic ions eject atoms from target to space and take them to condense on the sample surface.

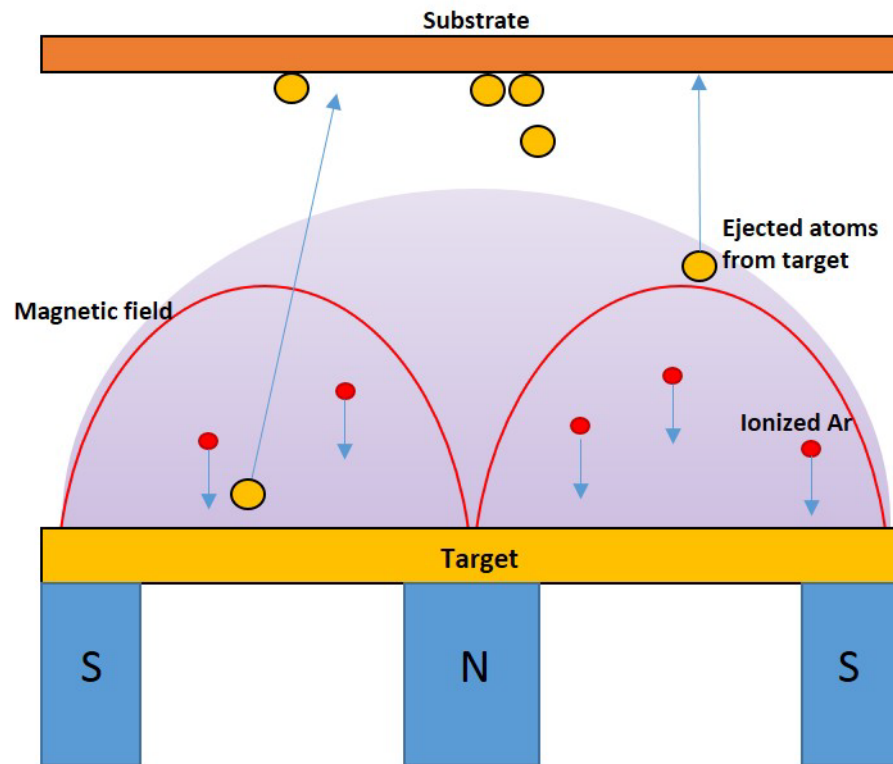


Fig. 2.7 Mechanism of magnetron sputtering deposition.

For magnetron sputtering deposition, a DC power (for conductive material deposition) is applied between the target and substrate to create plasma and accelerate Ar ions to bombard the target. In addition, a closed strong magnetic field is applied in front of the target to increase the deposition efficiency. The presence of a magnetic field paralleled to the target surface and the electric field perpendicular to the target together will drift the electrons in a circular path. This can increase the Ar gas ionization efficiency and lower the required Ar

pressure for initiating plasma, which can reduce the interruption from background Ar gas for the film fabrication. This can also keep the plasma cloud only close to the target area to prevent film being damaged from plasma. Parameters as Ar pressure, target and substrate distance, plasma power and deposition time can be adjusted to produce film with desired property like thickness and smoothness[13], [14].

### 2.32 Molecular Beam Epitaxy (MBE)

Molecular Beam Epitaxy[15] is a thin film deposition technique required to operate in UHV system. The deposition rate of MBE is relatively slower than other methods, such as PVD (several to hundreds Å per mins), and can be well controlled from less than 0.1 Å/min to more than 50Å /min. The slow deposition rate allows evaporated atoms epitaxy and layer by layer growth along the crystal lattice[16]. Fig. 2.8 shows the design of MBE and the slow deposition process. The material used for deposition can be metal rods or other shapes in a crucible. A filament is used to create electrons. A high voltage is applied between the filament and rods to draw electrons towards the metal rod. After the electrons hit the metal rods, all the high kinetic energy will convert to heat and raise the temperature of the metal rod to the evaporation point. Normally, The MBE system has several metal rods in separate evaporation cells for different metal deposition without opening the vacuum. The deposition rate can be controlled by monitoring the electron emission current from the filament and the flux current from metal rods. During the evaporation process, a very small amount of the vapor is ionized and is proportional to the total amount of vapor from metal rods. This flux current can be detected and used to get the perceived measurement of MBE deposition rate.

In order for crystal films to grow epitaxially, controlled appropriate substrate temperature is important. Low temperature can cause the atom to be directly attached to the surface and lose its mobility for rearrangement. Conversely, overly high temperatures can induce agglomeration of the deposited atoms, or reaction with the substrate.

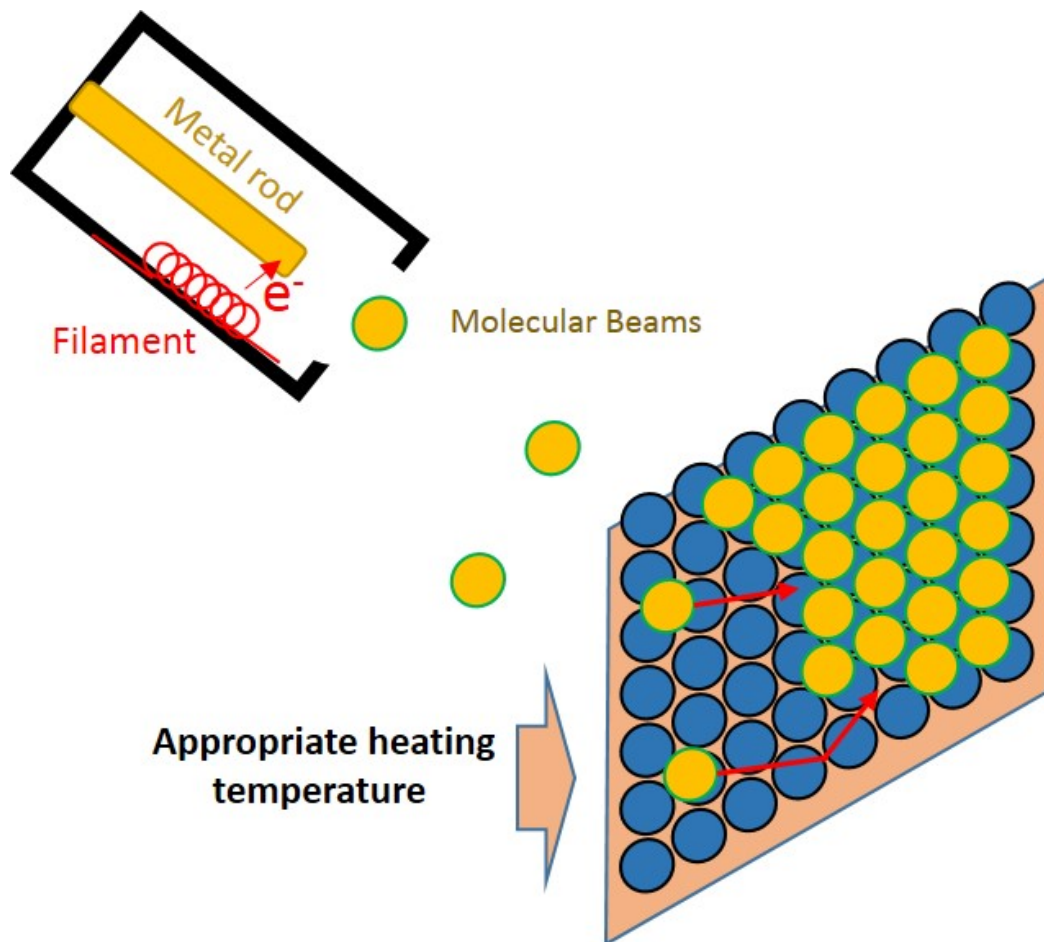


Fig. 2.8 Molecular beam epitaxy deposition.

High temperature can cause the atom to desorb from the surface and make the deposition rate very slow. With appropriate temperature, after the atom reaches the surface, it can migrate on the surface until it finds a proper position along the crystal lattice.

### 2.33 Atomic Force Microscopy (AFM)

Atomic force microscopy (AFM) is one type of scanning force microscopy with high resolution (from less than one nanometer to micrometers) for sample physical properties analysis. There are different operation modes of AFM. In order to acquire sample surface roughness, the image formation mode is used. The basic principle of AFM image operation is shown in Fig 2.9. The image is acquired by scanning the sample surface with a very sharp tip. The force between the tip and sample is changed according to the sample surface vertical height. The force is measured by a cantilever and laser. A laser beam is shot on the head of the cantilever and reflected to a position sensitive photodetector.

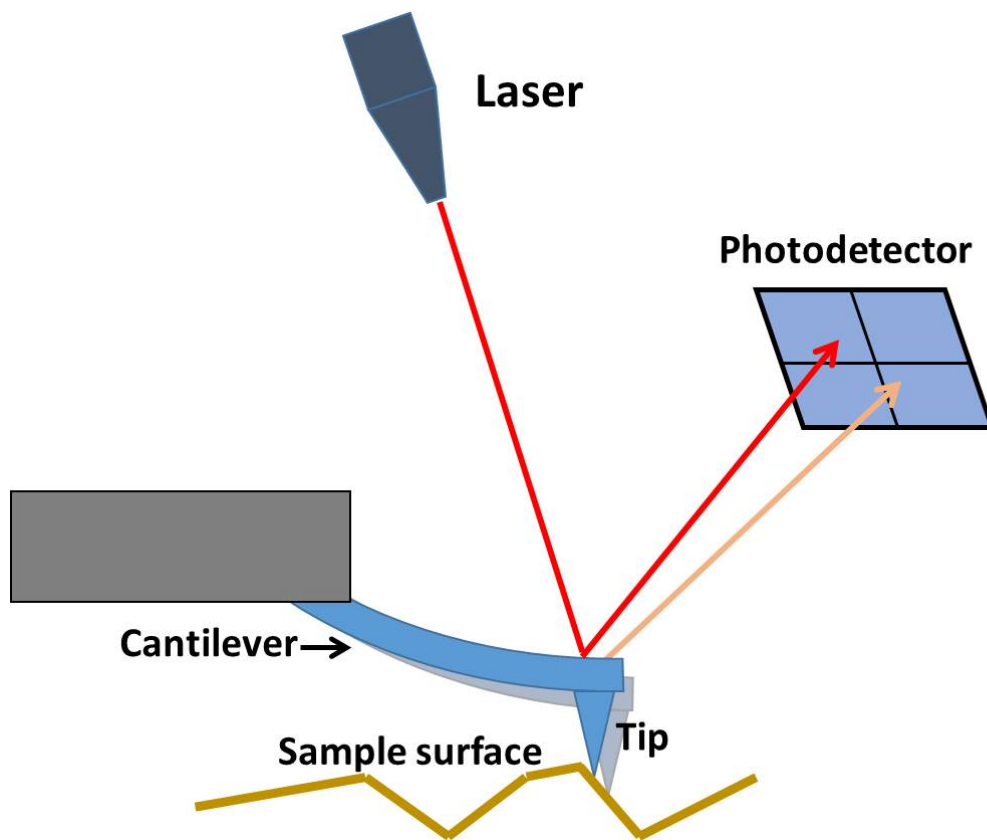


Fig.2.9 The basic principle of AFM image.

The total intensity of the layer is fixed. The position of the tip can be calculated by the intensity changes on different segments of the photodetector caused by the angular deflections of the laser beam from the cantilever. The height information of the sample surface is plotted as a color mapping (different color indicates different vertical height on the image) when tip scanning on the sample surface. The surface roughness can be acquired from the AFM image.



## CHAPTER 3

### EXPERIMENTAL RESULTS

The experiment results of Co (0001) film on  $\text{Al}_2\text{O}_3$ ,  $\text{Cr}_2\text{O}_3$  (111) on Co (0001) and  $\text{Cr}_2\text{O}_3$  (0001) on  $\text{Al}_2\text{O}_3$  (0001) fabrication are present in this section. All the film deposition occurred on 10mm x 10mm x 0.5mm  $\text{Al}_2\text{O}_3$  (0001) substrate, which is commercially available from Princeton Scientific Corporation. , Before insertion into UHV, all the  $\text{Al}_2\text{O}_3$  samples were first cleaned in acetone and ethanol separately by sonicator for 15 min, then rinsed by DI water for 10 times. After an  $\text{Al}_2\text{O}_3$  sample introduced to the UHV system, it was annealed at 1000K for 30mins to remove surface contamination, such as adventitious C.

#### 3.1 Magnetron Sputtering Deposition of Cobalt on $\text{Al}_2\text{O}_3$ (0001) Films

The experiment of thin film Co PVD deposition is operated in UHV System 2 (magnetron sputtering deposition chamber). For Co magnetron sputtering deposition, all Co samples were deposited at 800 K for 15mins (Cobalt has phase transition from fcc to bcc structure close to 773 K, in order for Cobalt to have hexagonal crystal pattern for next  $\text{Cr}_2\text{O}_3$ (0001) fabrication, we direct deposit Co at 800 K, which is above phase transition temperature to improve the crystal quality[8]). In order to optimize the surface smoothness of the Cobalt sample, deposition parameters such as different plasma power and Ar Pressure have been used for Co deposition. After deposition, a sample was taken out for ex situ AFM analysis and transferred to UHV system 3 for in situ XPS and LEED analysis.

### 3.11 Co Surface Roughness Improvement

After Co magnetron sputtering deposition with 50w plasma power and 15mtorr Ar pressure, AFM indicated the rms roughness for the film was about 3.7nm, which is too rough for thin  $\text{Cr}_2\text{O}_3$  film deposition on it. In order to find out if this is caused by the high background Ar gas interruption, we reduced the Ar pressure from 15mT to 7mT. After Co deposition at this pressure, AFM indicated the RMS value was reduced to about 0.78nm. Fig. 3.1 shows the AFM image of these two samples. Fig.3.1 (a) shows the Co is island growth on

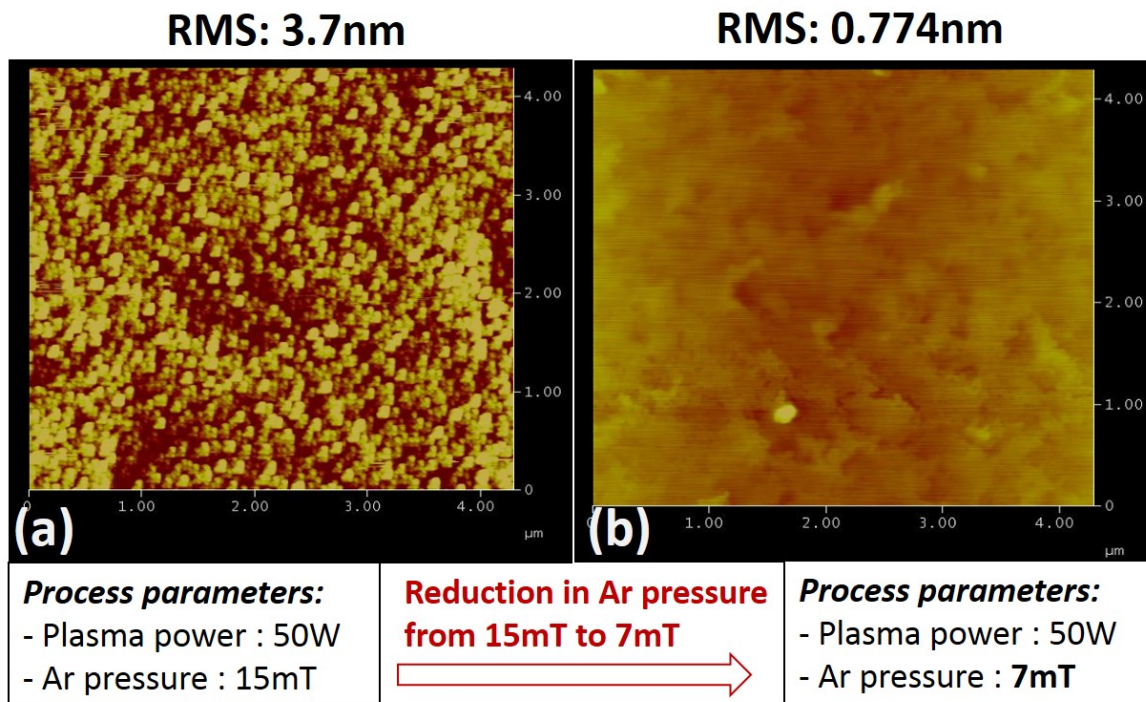


Figure. 3.1 The AFM image acquired after Co PVD deposition on  $\text{Al}_2\text{O}_3$  at 800K for 15mins with (a) plasma power at 50w and Ar pressure at 15mtorr and (b) plasma power at 50w and Ar pressure at 7mT.

$\text{Al}_2\text{O}_3$  substrate with 15mT Ar pressure. After reducing the Ar pressure to 7mT, Fig.3.1 (b) shows the Cobalt surface became much flatter. RMS values acquired from the AFM spectra

have been reduced from 3.7nm to 0.77nm indicate the surface is much smoother. After the reduction of surface roughness by reducing the Ar pressure, the the Ar pressure was lowered further to attempt to further reduce the surface roughness. After we reduced Ar pressure from 7mTorr to 3.5 mTorr, AFM indicated the surface roughness didn't change much and was still around 0.75nm. In order to see if the strength of plasma power also contributes to the film RMS roughness, Ar pressure was kept at 15mT and plasma power reduced to 15W, after making several samples for this parameter, the AFM indicates the rms roughness fluctuated from 0.7 to 1nm. After both reduced the Ar pressure to 3.5 mTorr (lowest Ar pressure we can keep to create plasma for Co deposition) and plasma power was reduced to 10 W, RMS was further reduced to 0.6nm. Fig.3. 2(a) shows the AFM spectra of Co deposition with 15W

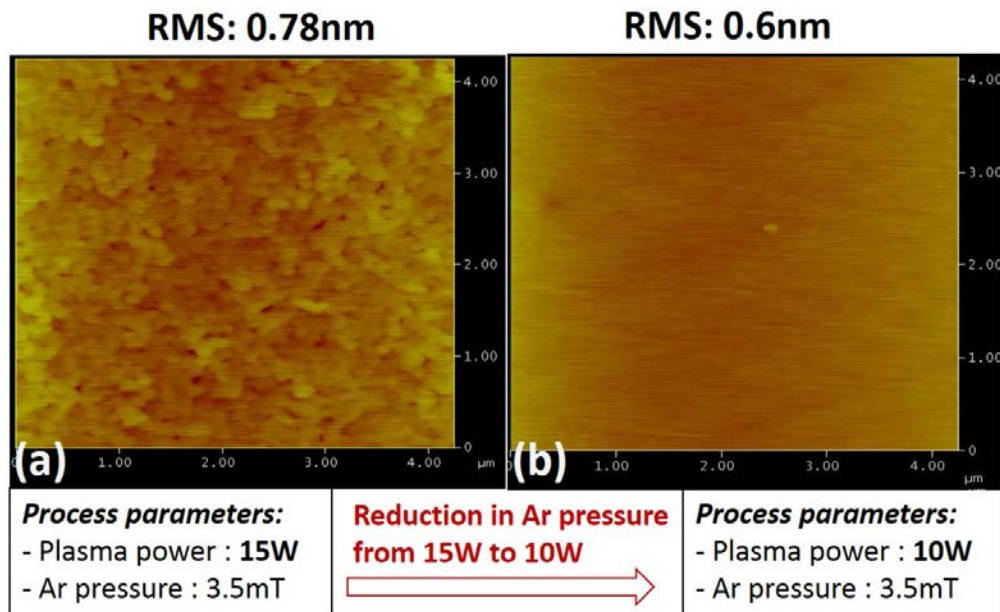


Figure. 3.2 The AFM image acquired after Co PVD deposition on Al<sub>2</sub>O<sub>3</sub> at 800K for 15mins with (a) plasma power at 15w and Ar pressure at 3.5mTorr and (b) plasma power at 10w and Ar pressure at 3.5mT.

plasma power and 3.5 mTorr Ar, The Co RMS roughness for this sample is about 0.78nm. After we reduced the power to 10W and kept Ar pressure at 3.5mT, AFM indicates there is an optimum parameter for smooth Co film deposition. As shown in Fig. 3.2 (b), after reducing the plasma power and Ar pressure from 15W, 3.5mT to 10w, 3.5mT, the surface smoothness was further improved. The RMS roughness reduced from 0.78nm to 0.6nm.

Table 1 shows the Co samples deposited by magnetron sputtering with different parameters and RMS roughness acquired by AFM. The first two samples show if you keep the plasma power the same and reduce the Ar Pressure from 15 to 7mT, the RMS significantly reduced from 3.7 to 0.778nm. The last two samples show if you keep the Ar pressure the same and reduce the plasma power from 15 to 10W, RMS was future reduced from 0.78 to 0.6nm. Between 15 to 50W and 7mT to 3.5 mT, AFM indicated the RMS roughness is fluctuated around 0.75 to 0.85nm and did not have significant improvement.

Type of films	Plasma power	Ar Pressure	Dep time	RMS
Co PVD	50W	15mT	15 mins	3.7nm
Co PVD	50W	7mT	15 mins	0.774nm
Co PVD	15W	3.5mT	15 mins	0.78nm
Co PVD	10W	3.5mT	15 mins	0.6nm

Table 3.1 List of sample RMS with corresponding experiment parameters after Co magnetron sputtering deposited Co (0001) on Al<sub>2</sub>O<sub>3</sub>. RMS is measured by AFM.

### 3.12 XPS and LEED Analysis

After the AFM analysis we transferred sample to UHV system 3 for XPS and LEED analysis. Fig.3.3 shows x-ray photoelectron spectroscopy (XPS) acquired from Co(0001) after

surface cleaning by the oxygen and hydrogen annealing (oxygen is used to remove carbon contamination followed by hydrogen to remove residual oxygen). The C (1s) and O (1s) spectra (Fig. 3.3 (a, b)) shows the surface are free of oxygen and carbon. Co (2p) spectra (Fig. 3.3 (c)) indicates the only peak present is Co (2p<sub>1/2</sub>) and Co (2p<sub>3/2</sub>) peak at 763.1eV and 778.1eV which are the Co (2p) split spin-orbit peaks. If Cobalt oxide is formed, the Co (II) and Co (III) peak and their satellite feature peaks with higher binding energy will be present in Co(2p) spectra which are not observed[17], [18]. All these XPS data indicate the Co sample surface is just pure metallic Co with no carbon and oxygen contamination. Fig. 3.4 (a) and (b) shows the LEED pattern corresponding to aluminum substrate after annealing in oxygen and Co (0001) overlayer after 15mins PVD deposition with 10W plasma power and 3.5mTorr Ar pressure. The LEED image 3.4 (a) for aluminum shows the inner array of 6 spots with three strong and weak intensities indicate the Al<sub>2</sub>O<sub>3</sub> (0001) C<sub>3v</sub> symmetry. The LEED spectrum looks blurry which is caused by charging problems from low energy electrons accumulation on aluminum sample surface caused by strong insulate property of Al<sub>2</sub>O<sub>3</sub>. The LEED image 7(b) for Cobalt shows 6 strong spots with C<sub>6v</sub> symmetry indicating the highly ordered Co(0001) crystal surface.

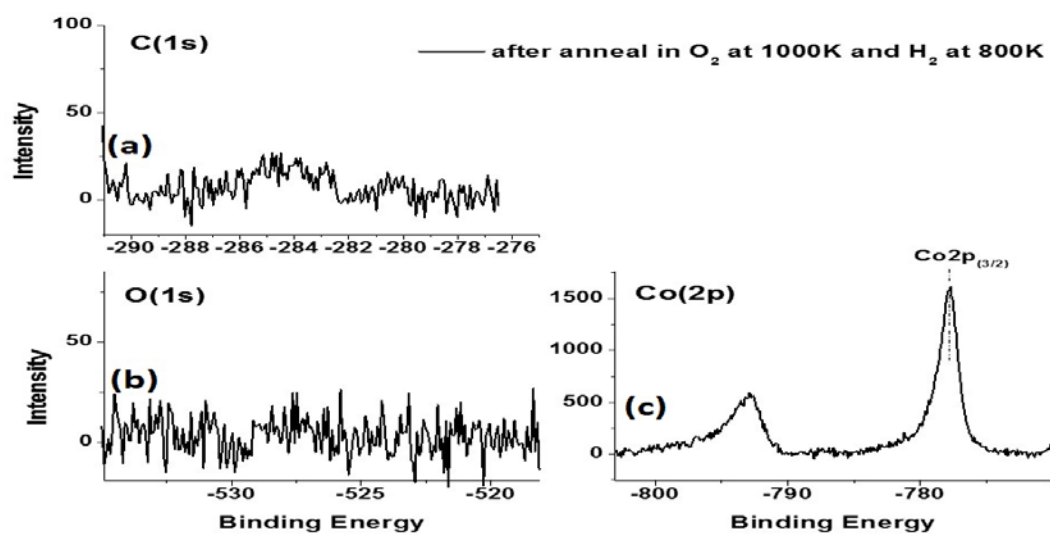


Fig. 3.3 The XPS Core level spectra for (a) C(1s), (b) O(1s) and (c) Co(2p) acquired after Co Cleaning process.

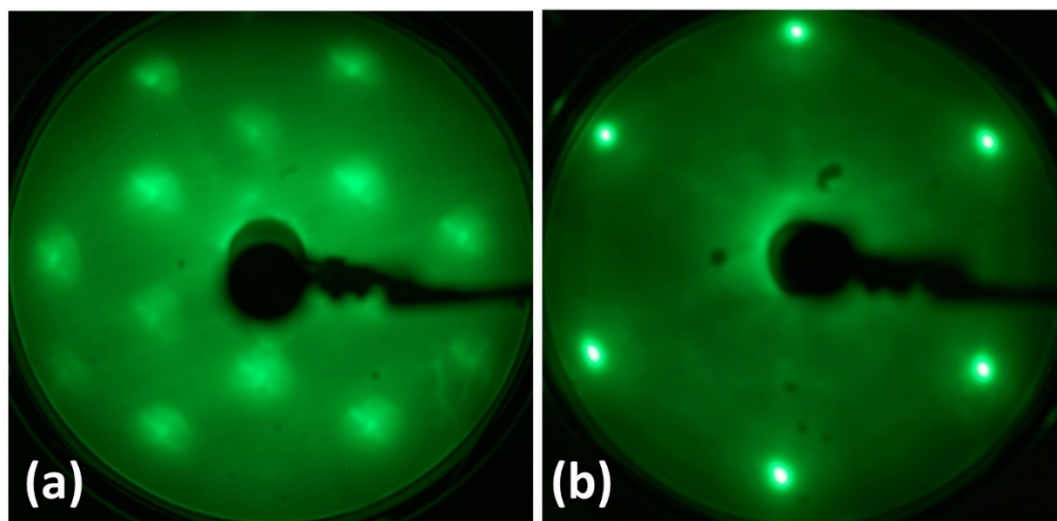


Fig. 3.4 LEED patterns for (a) clean  $Al_2O_3$  and (b) Co overlayers on  $Al_2O_3$ ; All LEED patterns acquired at 70 eV beam kinetic energy.

### 3.2 MBE of $\text{Cr}_2\text{O}_3$ on $\text{Co}(0001)/\text{Al}_2\text{O}_3$ Films<sup>1</sup>

The experiment of  $\text{Cr}_2\text{O}_3$  MBE deposition on  $\text{Co}(0001)$  was carried out in UHV system 1. Fig. 3.5 (a) displays Auger Electron Spectroscopy (AES) acquired after the first (solid line) and second (dashed line) Cr deposition/oxidation cycles on  $\text{Co}(0001)$ . The Cr(LMM) and O(KVV) spectra (Fig. 3.5 a, b) are consistent with  $\text{Cr}_2\text{O}_3$  [19], [20] and indicate an average chromia thickness of 9 Å after the first deposition/oxidation cycle, and 11 Å average thickness after the second deposition/oxidation cycle. This apparent change in deposition rate between cycles may be due in part to small variations in sample position and beam flux, but may also reflect a change in Cr sticking coefficient with chromia surface coverage.

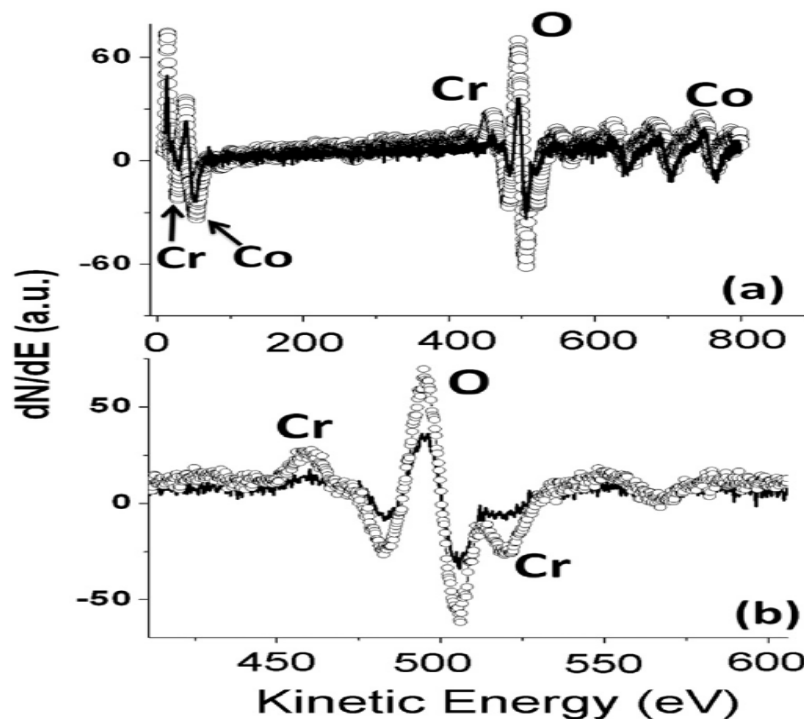


Fig. 3.5 (a) Auger electron spectroscopy acquired after 1st Cr MBE/oxidation cycle (solid black trace) and after 2nd Cr MBE/oxidation cycle (open circles), (b) the expanded view of the Cr (LMM)/O (KVV) region. (LMM is an L shell core hole, M shell transition and M shell Auger electron while KVV is a K shell core hole, transition from the valence band and valence band Auger electron).

<sup>1</sup> The section 3.2 of the chapter 3 is presented its entirety from "Ultrathin chromia films grown with preferential texture on metallic, semimetallic and insulating substrates," *Mater. Chem. Phys.*, vol. 149–150, pp. 113–123, 2015."



The corresponding low energy LEED image (Fig.3.6 a) and corresponding line scan (Fig.3.6 b) for the 9 Å chromia film consists of a faint outer six-fold array of diffraction spots, and a brighter inner array of six-fold LEED diffraction spots, both arrays having the same angular orientation. After the 2<sup>nd</sup> deposition, however, the LEED image (Fig.3.6 c) and corresponding line scan (Fig.3.6 d) across the LEED image, taken for 11 Å of chromia on Co(0001), indicate only the inner ring of LEED diffraction spots; the outer ring of LEED

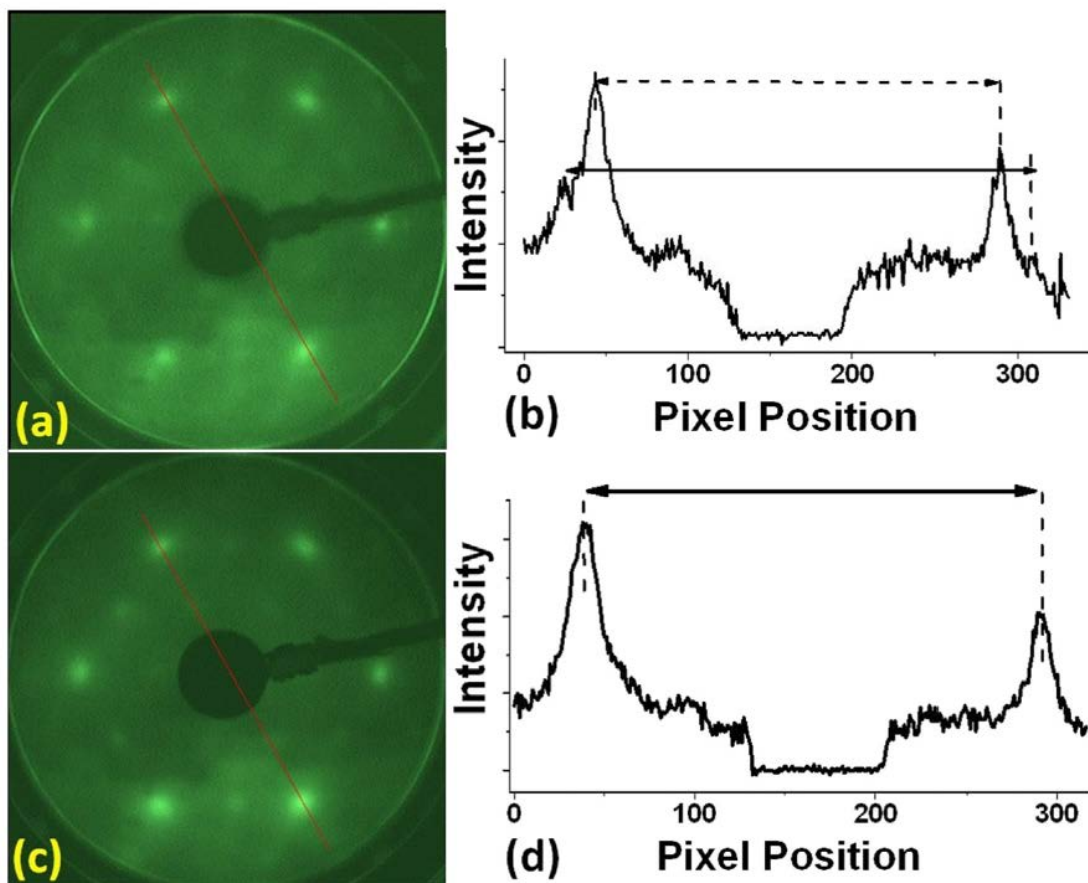


Fig. 3.6 The LEED image (a) and line scan (b) after the first chromium deposition/oxidation cycle (roughly 9 Å) on Co (0001). Note the evidence of overlayer mismatch in the line scan. This can be compared with the LEED image (c) and line scan (d) after diffraction spots has disappeared. This identifies the outer LEED diffraction spots in Fig. 3.6 (a) array as related to a six-fold



Co(0001) substrate and the inner LEED diffraction spots as corresponding to  $\text{Cr}_2\text{O}_3$ . The absence of substrate-related spots after the second deposition (Fig. 3.6 c, d) indicates that two deposition/oxidation cycles result in a continuous, epitaxial chromia film on Co(0001), much like that observed for chromia on Cu(111), as discussed above. The LEED patterns for chromia on Co(0001) (Fig. 3.6 a, c) do not, however, exhibit C3V symmetry, indicating that the film is not single-domain. From X-ray diffraction scans it is known that the chromia (0001) surfaces tend to have twin domains, and such twinning is likely, and a possible explanation for the 6 fold, rather than 3 fold, symmetry[21], [22]. These LEED images for chromia on Co(0001) (Fig. 3.6 a, c) are similar to those previously reported for  $\text{Cr}_2\text{O}_3$ (0001) films on Ag(111) [23]. Although there is a lattice mismatch ( $\text{Cr}_2\text{O}_3$ (0001): 4.96 Å [24], [25] Co(0001): 2.507 Å[26]), a comparison of chromia LEED diffraction spots, with those from the Co substrate (Fig. 3.6 a), indicate that lattice of the chromia overlayer and Co substrate are azimuthally aligned. The XPS Cr 2p and O 1s spectra of chromia ( $\text{Cr}_2\text{O}_3$ ) grown on Co(0001) are shown in Fig. 3.8 (a, b). The corresponding LEED image for the chromia/Co film, after a flash anneal in ultra-high vacuum(UHV), is shown in Fig. 3.7 (a), while that of a clean Co(0001) substrate acquired in the same chamber under the same experimental conditions is shown in Fig. 3.7 (b). Corresponding LEED images for the chromia film on  $\text{Al}_2\text{O}_3$ (0001), and the alumina substrate prior to chromia deposition, are shown in Fig. 3.10 (a, b) for comparison. The  $\text{Cr}_2\text{O}_3$ (0001)/Co(0001) LEED diffraction image (Fig. 3.6 c) is stable after exposure to air, transfer and annealing Fig. 3.7 (a), so even for a more reactive substrate like Co(0001), sample transfer will not significantly disrupt the long range order of the chromia film. As shown in Fig. 3.8 (a, b), the XPS Cr 2p<sub>3/2</sub> and O 1s spectra, for the ~11 Å thick chromia films on Co(0001) exhibit peak maxima at binding energies of 575.7 eV and 529.6 eV,

rather smaller than those observed for chromia on most other substrates [27]. For chromia on Co(0001) experiments, the XPS peaks were referenced to a metallic Co 2p<sub>3/2</sub> peak binding energy of 778.1 eV [28], [29] obtained from the ~1000 Å thick Co substrate. These data exhibit core level binding energies greater than those observed for chromia on sapphire (Fig. 3.8 c, d).

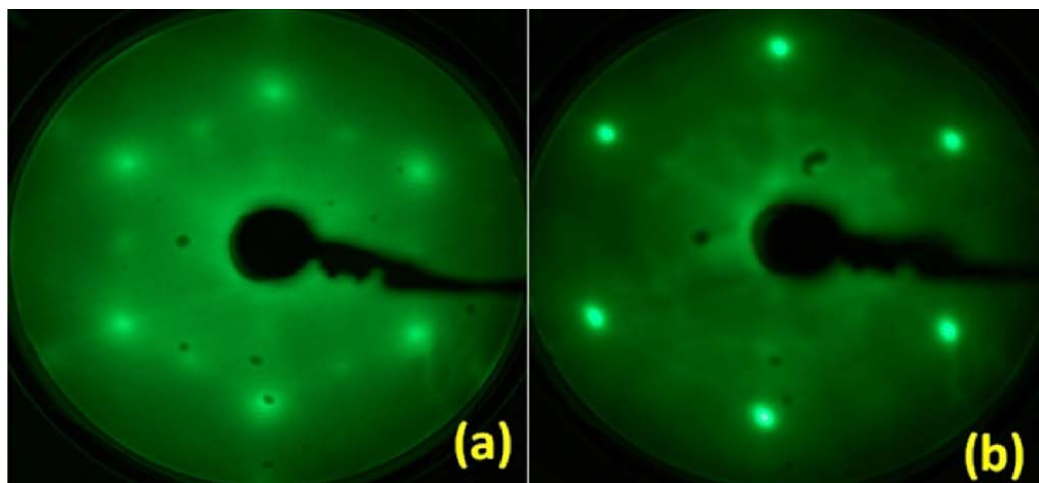


Fig. 3.7 The various LEED patterns for chromia overlayers on cobalt: (a) thicker (>11 Å) Cr<sub>2</sub>O<sub>3</sub> on Co; (b) the clean Co substrate; All LEED patterns acquired at 90 eV beam kinetic energy.

For chromia on Al<sub>2</sub>O<sub>3</sub>, the core level photoemission peaks were referenced with respect to the Al 2p<sub>3/2</sub> peak at 74.7 eV [29], [30], but there is considerable uncertainty as to the correct Al 2p reference binding energy because this is a dielectric substrate and is reflected by the range of binding energies reported from 73.5 eV [31], to 73.7 eV [32], to 74.1 eV [33], to 74.9 eV [28]. Thus, there is no certainty that the greater binding energy is due to the dielectric substrate or the greater chromia film thickness. The XPS indicates the average thickness of the Cr<sub>2</sub>O<sub>3</sub> film on alumina is 25 Å. The thicker chromia film on alumina exhibits higher binding energies compared to the 11 Å thick Cr<sub>2</sub>O<sub>3</sub> film on Co(0001).

The Co 2p XPS spectra for the Cr<sub>2</sub>O<sub>3</sub>/Co(0001) film (Fig. 3.9) also shows a high binding

energy shoulder, indicating the presence of an interfacial Co oxide with an average thickness of 3.5 Å. This oxide layer showed no change upon subsequent sample exposures to ambient air and annealing in UHV, providing additional evidence for the continuity of the chromia overlayer.

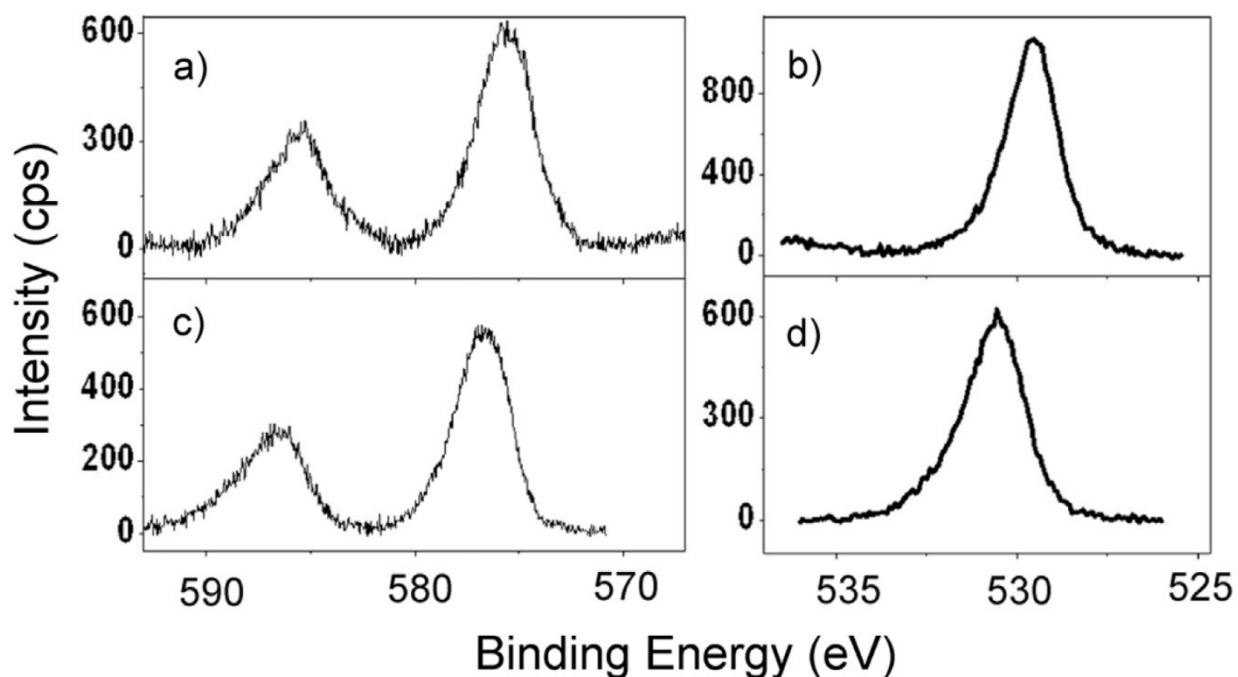


Fig. 3.8 The XPS core level spectra for Cr 2p (a) and O 1s (b) core levels after Cr<sub>2</sub>O<sub>3</sub> deposition on Co(0001) (see text), and for Cr 2p (c) and O 1s (c) core levels after Cr<sub>2</sub>O<sub>3</sub> deposition on Al<sub>2</sub>O<sub>3</sub>.

This is consistent with our observation that the Cr<sub>2</sub>O<sub>3</sub>(0001)/Co(0001) LEED diffraction images, are stable after exposure to air, during transfer, and subsequent annealing, so even for a more reactive substrate like Co(0001), sample transfer will not significantly disrupt the long range order of the chromia film. This interfacial oxidation at the cobalt to chromia interface has also been seen for cobalt deposition on chromia [34] and could contribute to the formation of chromia twinning and loss of C<sub>3v</sub> symmetry.

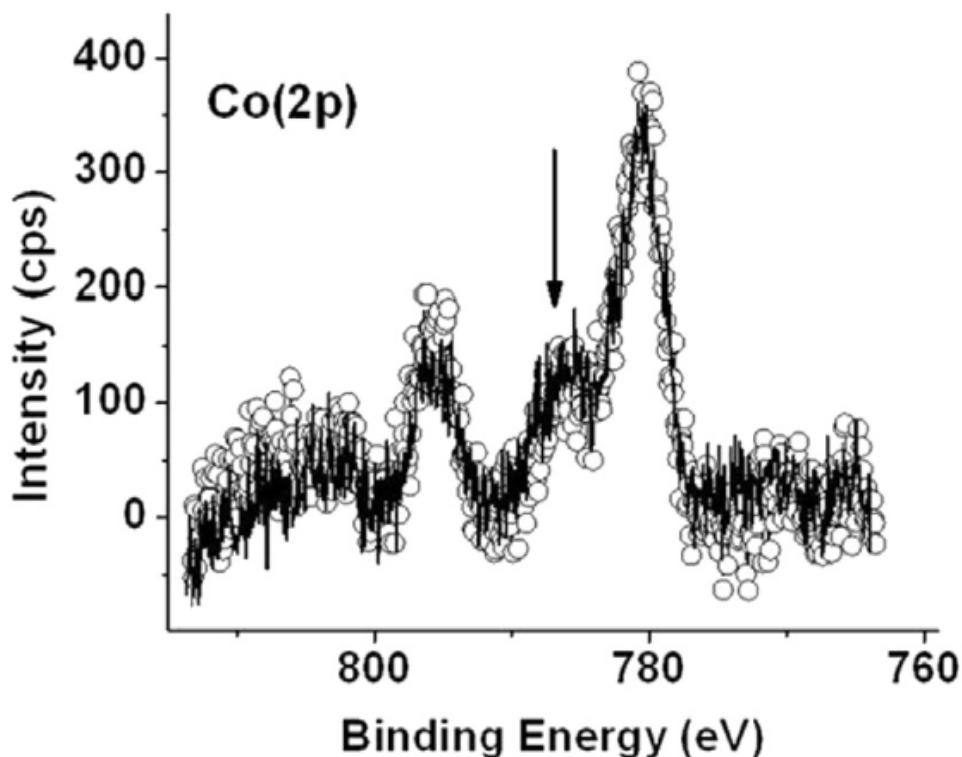


Fig. 3.9 XPS Co 2p spectra of a Cr<sub>2</sub>O<sub>3</sub> (0001)/Co (0001) film after sample transfer/UHV anneal (solid trace) and after a second air exposure/UHV annealing cycle (open cycle). The feature corresponding to the presence of cobalt oxide is marked by an arrow.

### 3.3 Chromia growth on Al<sub>2</sub>O<sub>3</sub> (0001)<sup>2</sup>

It should be noted that sapphire is the frequent substrate of choice [35], [36], [37]–[40] for chromia growth because of the close lattice match to  $\alpha$ -Al<sub>2</sub>O<sub>3</sub> (0001) substrate. This is borne out in our LEED studies as well. The LEED image for the chromia/alumina film (Fig. 3.10 a) exhibits C3V symmetry, indicating that the film grown on alumina occurs in a single domain film, or at least twinning of the chromia is vastly suppressed and that the chromia lattice is aligned with that of the Al<sub>2</sub>O<sub>3</sub>(0001) substrate, as noted by many previous investigators [35], [36], [37]–[40]. This is in contrast to LEED images for Cr<sub>2</sub>O<sub>3</sub> (0001)/Co (0001) (Fig. 3.6 C and 3.7

<sup>2</sup> The section 3.3 of the chapter 3 is presented its entirety from “Ultrathin chromia films grown with preferential texture on metallic, semimetallic and insulating substrates,” *Mater. Chem. Phys.*, vol. 149–150, pp. 113–123, 2015.”

a), that exhibit six-fold symmetry. This indicates that the chromia film grown on alumina is single domain, but the films grown on Co almost certainly are not single domain. It is clear that a lattice match for chromia growth, with regard to the substrate, is not essential. In particular, the lattice match for chromia growth on  $\text{Al}_2\text{O}_3$  (0001) is not perfect and thicker chromia films do not share the same lattice constant with the alumina substrate [41].

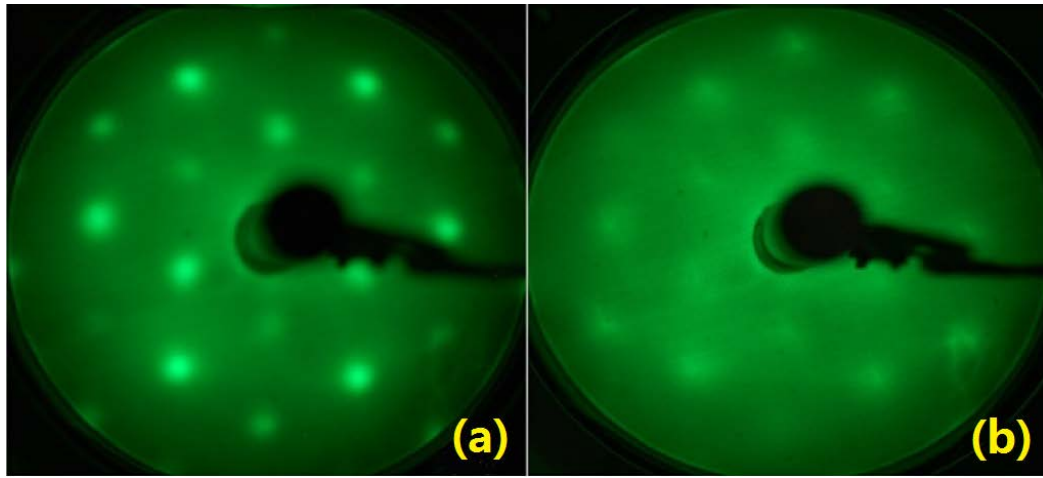


Fig. 3.10 The various LEED patterns for chromia overlays on sapphire: (a)  $\text{Cr}_2\text{O}_3$  on  $\text{Al}_2\text{O}_3$  (b) the clean  $\text{Al}_2\text{O}_3$  substrate; All LEED patterns acquired at 90 eV beam kinetic energy.

## CHAPTER 4

### SUMMARY AND CONCLUSION

#### 4.1 Summary

Co (0001) texture growth on  $\text{Al}_2\text{O}_3$  (0001) is achieved by PVD deposition. AFM spectral shows the Co surface RMS roughness can be reduced from several nanometers to 0.6nm by optimizing the plasma power and Ar pressure for magnetron sputtering deposition. XPS and LEED data demonstrates the pure metallic cobalt formation with zero contamination after oxygen and hydrogen cleaning process in ultrahigh vacuum and Co(0001) crystal formation with very sharp  $\text{C}_{6v}$  LEED pattern.

$\text{Cr}_2\text{O}_3$ (0001) films can be successfully fabricated on Co (0001) and  $\text{Al}_2\text{O}_3$  (0001) substrates, Cr deposition and oxidation on Co (0001) and provides a thin  $\text{Cr}_2\text{O}_3$  layer with average thickness about 11 Å. Even if not epitaxial, it is stable above 1000K in ultra-high vacuum (UHV), but accompanied by the formation of a 3.5 Å interfacial Co layer. The orientation of the Chromia lattice was aligned with Co (0001) and  $\text{Al}_2\text{O}_3$  substrates even with a lattice mismatch.

Cr deposition/oxidation on Co (0001) provides a  $\text{Cr}_2\text{O}_3$  layer ~11 Å average thickness, even if not epitaxial, stable to >1000 K in ultra-high vacuum (UHV), but accompanied by the formation of an interfacial Co oxide layer ~3.5 Å thick. The orientation of the chromia lattice was aligned with that of the substrate, in spite of a lattice mismatch. The XPS and LEED data indicate ultrathin continuous epitaxial chromia can be grown on Co (0001) and  $\text{Al}_2\text{O}_3$ (0001) substrates. The XPS and LEED data also indicate the  $\text{Cr}_2\text{O}_3$  films are stable even after above 1000K annealing in UHV, and survive exposure to ambient without significant change to

chemical composition or long range order. These excellent properties show the high practicality of the  $\text{Cr}_2\text{O}_3$  films for spintronics and other applications.

#### 4.2 Future work

Further work needs to be done for the research of materials towards voltage control of spintronics. As  $\text{Cr}_2\text{O}_3$  (0001) films can be successfully grown on Co(0001) films even with a lattice mismatch, can we grow a third layer on  $\text{Cr}_2\text{O}_3$  films, such as graphene, which has huge potential to be used for spintronics, still needs to be explored. Fabrication of  $\text{Cr}_2\text{O}_3$  (0001) film on other ferromagnetic material also needs to be investigated. The low coercivity of Co (0001) thin films, which has its limitations to be used for spintronics, more research is needed to explore other possible substrates for  $\text{Cr}_2\text{O}_3$  (0001)

## REFERENCES

- [1] W. Eerenstein, N. D. Mathur, and J. F. Scott, "Multiferroic and magnetoelectric materials.," *Nature*, vol. 442, no. 7104, pp. 759–65, Aug. 2006.
- [2] G. T. Rado, "Mechanism of the Magnetoelectric," vol. 6, no. 11, pp. 609–610, 1961.
- [3] W. Echtenkamp and C. Binek, "Electric control of exchange bias training," *Phys. Rev. Lett.*, vol. 111, no. 18, pp. 1–5, 2013.
- [4] W. Kleemann, "Magnetoelectric spintronics," *J. Appl. Phys.*, vol. 114, no. 2, pp. 1–4, 2013.
- [5] C. Binek and B. Doudin, "Magnetoelectronics with magnetoelectrics," *J. Phys. Condens. Matter*, vol. 17, no. 2, pp. L39–L44, 2005.
- [6] S. P. Pati, N. Shimomura, T. Nozaki, T. Shibata, and M. Sahashi, "Néel temperature of Cr<sub>2</sub>O<sub>3</sub> in Cr<sub>2</sub>O<sub>3</sub>/Co exchange-coupled system: Effect of buffer layer," *J. Appl. Phys.*, vol. 117, no. 17, p. 17D137, May 2015.
- [7] X. He, Y. Wang, N. Wu, A. N. Caruso, E. Vescovo, K. D. Belashchenko, P. a Dowben, and C. Binek, "Robust isothermal electric control of exchange bias at room temperature.," *Nat. Mater.*, vol. 9, no. 7, pp. 579–585, 2010.



- [8] W. Kuch, L. I. Chelaru, F. Offi, J. Wang, M. Kotsugi, and J. Kirschner, "Tuning the magnetic coupling across ultrathin antiferromagnetic films by controlling atomic-scale roughness.," *Nat. Mater.*, vol. 5, no. 2, pp. 128–33, Feb. 2006.
- [9] N. Wu, X. He, A. L. Wysocki, U. Lanke, T. Komesu, K. D. Belashchenko, C. Binek, and P. a. Dowben, "Imaging and control of surface magnetization domains in a magnetoelectric antiferromagnet," *Phys. Rev. Lett.*, vol. 106, no. 8, pp. 17–20, 2011.
- [10] M. P. S. D. Briggs, *Practical surface analysis, 2nd edn., vol I, auger and X-ray photoelectron spectroscopy. Edited by D. Briggs & M. P. Seah, John Wiley, New York, 1990, 657 pp., price: £86.50. ISBN 0471 92081 9.* 1990.
- [11] S. Tanuma, C. J. Powell, and D. R. Penn, "Calculations of electron inelastic mean free paths. V. Data for 14 organic compounds over the 50-2000 eV range," *Surf. Interface Anal.*, vol. 21, no. 3, pp. 165–176, Mar. 1994.
- [12] J. G. Han, "Recent progress in thin film processing by magnetron sputtering with plasma diagnostics," *J. Phys. D. Appl. Phys.*, vol. 42, no. 4, p. 043001, Feb. 2009.
- [13] J. Wang, E. Elamurugu, N. Franco, E. Alves, A. M. Botelho do Rego, G. Gonçalves, R. Martins, and E. Fortunato, "Influence of deposition pressure on N-doped ZnO films by RF magnetron sputtering.," *J. Nanosci. Nanotechnol.*, vol. 10, no. 4, pp. 2674–8, Apr. 2010.

- [14] Y. S. Jung, D. W. Lee, and D. Y. Jeon, "Influence of dc magnetron sputtering parameters on surface morphology of indium tin oxide thin films," *Appl. Surf. Sci.*, vol. 221, no. 1–4, pp. 136–142, Jan. 2004.
- [15] W. P. McCray, "MBE deserves a place in the history books.," *Nat. Nanotechnol.*, vol. 2, no. 5, pp. 259–61, May 2007.
- [16] V. A. Shchukin and D. Bimberg, "Spontaneous ordering of nanostructures on crystal surfaces," *Rev. Mod. Phys.*, vol. 71, no. 4, pp. 1125–1171, Jul. 1999.
- [17] J. Yang, H. Liu, W. N. Martens, and R. L. Frost, "Synthesis and Characterization of Cobalt Hydroxide, Cobalt Oxyhydroxide, and Cobalt Oxide Nanodiscs," *J. Phys. Chem. C*, vol. 114, no. 1, pp. 111–119, Jan. 2010.
- [18] M. C. Biesinger, B. P. Payne, A. P. Grosvenor, L. W. M. Lau, A. R. Gerson, and R. S. C. Smart, "Resolving surface chemical states in XPS analysis of first row transition metals, oxides and hydroxides: Cr, Mn, Fe, Co and Ni," *Appl. Surf. Sci.*, vol. 257, no. 7, pp. 2717–2730, 2011.
- [19] A. Velon and D.-Q. Yi, "Influence of Cr on the Oxidation of Fe<sub>3</sub>Al and Ni<sub>3</sub>Al at 500°C," *Oxid. Met.*, vol. 57, no. 1–2, pp. 13–31.
- [20] A. Picone, G. Fratesi, M. Riva, G. Bussetti, A. Calloni, A. Brambilla, M. I. Trioni, L. Duò, F. Ciccacci, and M. Finazzi, "Self-organized chromium oxide monolayers on Fe(001)," *Phys. Rev. B*, vol. 87, no. 8, p. 085403, Feb. 2013.

- [21] M. W. Herdiech, X. Zhu, M. D. Morales-Acosta, F. J. Walker, and E. I. Altman, "The modification of ferroelectric LiNbO<sub>3</sub>(0001) surfaces using chromium oxide thin films," *Phys. Chem. Chem. Phys.*, vol. 17, no. 14, pp. 9488–98, Apr. 2015.
- [22] S. Punugupati, J. Narayan, and F. Hunte, "Strain induced ferromagnetism in epitaxial Cr<sub>2</sub>O<sub>3</sub> thin films integrated on Si(001)," *Appl. Phys. Lett.*, vol. 105, no. 13, p. 132401, Sep. 2014.
- [23] W. A. A. Priyantha and G. D. Waddill, "Structure of chromium oxide ultrathin films on Ag(111)," *Surf. Sci.*, vol. 578, no. 1–3, pp. 149–161, Mar. 2005.
- [24] O. Madelung, U. Rössler, and M. Schulz, Eds., *Non-Tetrahedrally Bonded Binary Compounds II*, vol. 41D. Berlin/Heidelberg: Springer-Verlag, 2000.
- [25] E. D. V. S. S and E. D. V. S. S, "Magnetic properties of Cr<sub>2</sub>O<sub>3</sub> Nanoparticles," *J. Magn. Magn. Mater.*, vol. 43, no. 6, pp. 1–3, 2003.
- [26] *Interfacial electrochemistry : theory, experiment, and applications* /. New York : Marcel Dekker, 1999.
- [27] X. Chen, H. Kazi, Y. Cao, B. Dong, F. L. Pasquale, J. a. Colón Santana, S. Cao, M. Street, R. Welch, C. Binek, A. Enders, J. a. Kelber, and P. a. Dowben, "Ultrathin chromia films grown with preferential texture on metallic, semimetallic and insulating substrates," *Mater. Chem. Phys.*, vol. 149–150, pp. 113–123, 2015.

- [28] S. A. Chambers, T. Droubay, D. R. Jennison, and T. R. Mattsson, "Laminar growth of ultrathin metal films on metal oxides: Co on hydroxylated alpha-Al<sub>2</sub>O<sub>3</sub>(0001).," *Science*, vol. 297, no. 5582, pp. 827–31, Aug. 2002.
- [29] "No Title." [Online]. Available: <http://srdata.nist.gov/XPS>.
- [30] C. D. Wagner, "X-ray photoelectron spectroscopy with x-ray photons of higher energy," *J. Vac. Sci. Technol.*, vol. 15, no. 2, p. 518, Mar. 1978.
- [31] C. D. Wagner, "Auger and photoelectron line energy relationships in aluminum–oxygen and silicon–oxygen compounds," *J. Vac. Sci. Technol.*, vol. 21, no. 4, p. 933, Nov. 1982.
- [32] H. M. Liao, "Surface composition of AlN powders studied by x-ray photoelectron spectroscopy and bremsstrahlung-excited Auger electron spectroscopy," *J. Vac. Sci. Technol. A Vacuum, Surfaces, Film.*, vol. 11, no. 5, p. 2681, Sep. 1993.
- [33] D. Leinen, A. Fernández, J. P. Espinós, J. P. Holgado, and A. R. González-Elipé, "An XPS study of the mixing effects induced by ion bombardment in composite oxides," *Appl. Surf. Sci.*, vol. 68, no. 4, pp. 453–459, Aug. 1993.
- [34] R. Cheng, C. N. Borca, N. Pilet, B. Xu, L. Yuan, B. Doudin, S. H. Liou, and P. A. Dowben, "Oxidation of metals at the chromium oxide interface," *Appl. Phys. Lett.*, vol. 81, no. 11, p. 2109, Sep. 2002.

- [35] M. A. Henderson, "Photochemistry of methyl bromide on the  $\alpha$ -Cr<sub>2</sub>O<sub>3</sub>(0001) surface," *Surf. Sci.*, vol. 604, no. 19–20, pp. 1800–1807, Sep. 2010.
- [36] M. A. Henderson and K. M. Rosso, "Oxidation of H<sub>2</sub>S by coadsorbed oxygen on the  $\alpha$ -Cr<sub>2</sub>O<sub>3</sub>(0001) surface," *Surf. Sci.*, vol. 605, no. 5–6, pp. 555–563, Mar. 2011.
- [37] S. A. Chambers, J. R. Williams, M. A. Henderson, A. G. Joly, M. Varela, and S. J. Pennycook, "Structure, band offsets and photochemistry at epitaxial  $\alpha$ -Cr<sub>2</sub>O<sub>3</sub>/ $\alpha$ -Fe<sub>2</sub>O<sub>3</sub> heterojunctions," *Surf. Sci.*, vol. 587, no. 3, pp. L197–L207, Aug. 2005.
- [38] M. A. Henderson and S. A. Chambers, "HREELS, TPD and XPS study of the interaction of water with the  $\alpha$ -Cr<sub>2</sub>O<sub>3</sub>(001) surface," *Surf. Sci.*, vol. 449, no. 1–3, pp. 135–150, Mar. 2000.
- [39] T. C. Kaspar, S. E. Chamberlin, and S. A. Chambers, "Surface structure of  $\alpha$ -Cr<sub>2</sub>O<sub>3</sub>(0001) after activated oxygen exposure," *Surf. Sci.*, vol. 618, pp. 159–166, Dec. 2013.
- [40] N. Iwata, T. Kuroda, and H. Yamamoto, "Mechanism of Growth of Cr<sub>2</sub>O<sub>3</sub> Thin Films on Sapphire Substrates by Direct Current–Radio Frequency Magnetron Sputtering," *Jpn. J. Appl. Phys.*, vol. 51, no. 11S, p. 11PG12, Nov. 2012.

[41] M. Street, W. Echtenkamp, T. Komesu, S. Cao, P. A. Dowben, and C. Binek, "Increasing the Néel temperature of magnetoelectric chromia for voltage-controlled spintronics," *Appl. Phys. Lett.*, vol. 104, no. 22, p. 222402, Jun. 2014.